Femtochemistry of *trans*-Azomethane: A Combined Experimental and Theoretical Study

Eric W.-G. Diau[a, b] and Ahmed H. Zewail*[a]

The dissociation dynamics of trans*-azomethane upon excitation to the $S_1(n,\pi^*)$ state with a total energy of 93 kcal mol^{-1} is investigated using femtosecond-resolved mass spectrometry in a molecular beam. The transient signal shows an opposite pump–probe excitation feature for the UV (307 nm) and the visible (615 nm) pulses at the perpendicular polarization in comparison with the signal obtained at the parallel polarization: The one-photon symmetry-forbidden process excited by the UV pulse is dominant at the perpendicular polarization, whereas the two-photon symmetry-allowed process initiated by the visible pulse prevails at the parallel polarization. At the perpendicular polarization, we found that the two C–N bonds of the molecule break in a stepwise manner, that is, the first C–N bond breaks in $\approx$70 fs followed by the second one in $\approx$100 fs, with the intermediate characterized. At the parallel polarization, the first C–N bond cleavage was found to occur in 100 fs with the intensity of the symmetry-allowed transition being one order of magnitude greater than the intensity of the symmetry-forbidden transition at the perpendicular polarization. Theoretical calculations using time-dependent density functional theory (TDDFT) and the complete active space self-consistent field (CASSCF) method have been carried out to characterize the potential energy surface for the ground state, the low-lying excited states, and the cationic ground state at various levels of theory. Combining the experimental and theoretical results, we identified the elementary steps in the mechanism: The initial driving force of the ultrafast bond-breaking process of* trans*-azomethane (at the perpendicular polarization) is due to the CNNC torsional motion initiated by the vibronic coupling through an intensity-borrowing mechanism for the symmetry-forbidden $n-\pi^*$ transition. Following this torsional motion and the associated molecular symmetry breaking, an S_0/S_1 conical intersection (CI) can be reached at a torsional angle of 93.1° (predicted at the CASSCF(8,7)/cc-pVDZ level of theory). Funneling through the S_0/S_1 CI could activate the asymmetric C–N stretching motion, which is the key motion for the consecutive C–N bond breakages on the femtosecond time scale.*

KEYWORDS:

ab initio calculations · azomethane · conical intersections · femtochemistry · mass spectrometry

1. Introduction

Because the reaction leads to an efficient nitrogen extrusion and produces two methyl radicals with a quantum yield close to unity,[1, 2] in many applications the photodissociation of *trans*-azomethane (AZM) has served as a clean source of free radicals.[3–6] Two different reaction mechanisms have been considered:[4, 7, 8] The energetic molecule breaks its two identical C–N bonds in a single step, a concerted mechanism; or, alternatively, it cleaves the C–N bonds in a stepwise manner. For the latter, the breakage of the two C–N bonds occurs on different time scales, and an intermediate (the CH_3N_2 radical) must be involved after the first bond breakage (Scheme 1). Both stepwise and concerted mechanisms have been suggested and the conclusion reached was from different experimental results—time-resolved coherent anti-Stokes Raman spectroscopy (CARS)[9] and photofragment translational spectroscopy (PTS)[10] (see below). The different conclusions have attracted many experimental[11–14] as well as theoretical[15–17] investigations on the fundamental issue of this mechanism.

The first absorption band of AZM, that is, the $S_0 \rightarrow S_1$ transition, has been understood to involve a perpendicular electronic excitation from the nonbonding n orbital of the nitrogen atoms to the antibonding π^* orbital.[16, 18, 19] This $n-\pi^*$ transition ($\tilde{A}^1B_g \leftarrow \tilde{X}^1A_g$), according to group theory, is strictly symmetry-

Concerted mechanism :

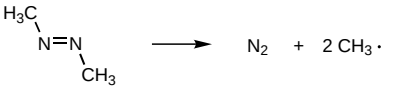

Stepwise mechanism :

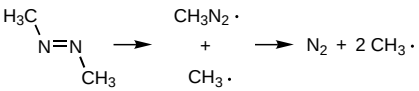

Scheme 1. *Concerted versus stepwise dissociation mechanism of azomethane.*

[a] *Prof. Dr. A. H. Zewail, Dr. E. W.-G. Diau*
Arthur Amos Noyes Laboratory of Chemical Physics
California Institute of Technology
Pasadena, California 91125 (USA)
Fax: (+1) 626-792-8456
E-mail: zewail@caltech.edu

[b] *Dr. E. W.-G. Diau*
Current address:
Department of Applied Chemistry
National Chiao Tung University
Hsinchu, Taiwan 30050 (Republic of China)
E-mail: diau@mail.ac.nctu.edu.tw

 DOI: 10.1002/cphc.200200579

forbidden for all *trans* azo compounds with C_{2h} symmetry.[20] Thus, the first absorption band of AZM shows a weak and broad spectral feature in the wavelength range from 270 nm to 410 nm, with the maximum intensity around 340 nm;[3] the intensity may be "borrowed" from higher-lying symmetry-allowed transitions through vibronic coupling, as in the case of acetone.[21] In fact, there are three high-energy strong absorption bands observed in the wavelength region of 140 – 200 nm (6 – 9 eV),[18] and they have been assigned to the $^1A_g \rightarrow {}^1B_u$ excitations which may be responsible for the symmetry-allowed transitions that give rise to the borrowed intensity for the forbidden $^1A_g \rightarrow {}^1B_g$ transition.[20] Furthermore, the S_1 spectrum of AZM shows essentially no vibrational structure.[3] The lack of observable fluorescence[20] might be due to a very efficient photoreaction in the $S_1(n,\pi^*)$ state.

Using the nanosecond time-resolved CARS technique, Weisman and co-workers[9] have studied the photodissociation dynamics of AZM for excitation at 355 nm in a static gas sample cell. Under the collisional conditions of the experiments, the authors used a multistep kinetic model to account for the behavior of both N_2 and cold CH_3 photoproducts and inferred the presence of the intermediate CH_3N_2 radical, with a lifetime of 5.3 ± 1 ns: a stepwise mechanism. Lee and co-workers[10] studied the photodissociation dynamics of this molecule using the technique of PTS for excitation at 351 nm in a molecular beam and found that the CH_3N_2 intermediate is actually short-lived in nature with a lifetime shorter than a rotational period ($\approx$ a picosecond). Judging from the isotropic distribution of the fragments, that is, the anisotropy parameter $\beta \approx 0$, the lifetime of the excited parent molecule was inferred to be longer than many rotational periods, thus it is not feasible to clock the second C–N bond cleavage in real time. Because the time-of-flight (TOF) spectra of the CH_3 fragments show a bimodal velocity distribution and the asymptotic center-of-mass velocity vectors of all three photofragments are strongly correlated, an asynchronous concerted C–N bond-breaking mechanism was suggested; the rotational period was used as a clock to define concertedness in the three-body dissociation of symmetric molecules.[22]

Two vibrational quantum-state-resolved studies[12, 13] have been carried out using resonantly-enhanced multiphoton ionization (REMPI) coupled with TOF mass spectrometry to measure the vibrational as well as translational energy distributions of the CH_3 fragments. The results of Weitz and co-workers[12] indicate that the observed CH_3 fragments, analyzed by a barrier impulsive model (BIM),[23] are correlated with the second step of the photodissociation process, supporting the stepwise mechanism.[9] On the other hand, Lee and co-workers[13] revisited this reaction using the same technique as Weitz and co-workers[12] but with time (nanosecond) and kinetic energy resolutions. They found that the appearance times for both CH_3 radical vibrational states were actually faster than the instrument response time (a few nanoseconds) and the vibrational-state-resolved translational energy distributions of the CH_3 fragments all showed a bimodal structure—this feature does not support the asynchronous concerted mechanism previously proposed.[10]

An early single determinant semiempirical study[19] qualitatively described the shape of the $S_1(n,\pi^*)$ potential energy surface (PES) of azomethane along several isomerization pathways, from *trans*- to *cis*-isomers, and suggested that the rotation about the N=N double bond is important. High-level ab initio calculations were recently performed by Morokuma and co-workers,[16] based on complete active space self-consistent-field (CASSCF) and multireference configuration interaction with single and double excitation (MRCISD) methods. The results have further confirmed that the S_0 and S_1 potential energy curves indeed come close along the CNNC torsional coordinate. With calculations at the CASSCF(6,4)/DZP level of theory, a conical intersection (CI) was found to have an asymmetrical structure with a CNNC dihedral angle of 92.8° and two CNN angles of 132.0 and 115.6°. Based on the potential energy functions fitted from the ab initio calculations,[17a] classical trajectories plus surface hopping calculations for the photodissociation dynamics of azomethane have been carried out by Cattaneo and Persico.[17b] The trajectory simulations indicate that the $S_1 \rightarrow S_0$ internal conversion (IC) process occurs within 0.5 ps and the dissociation takes places exclusively on the S_0 PES. Moreover, both C–N bonds are broken within 1 ps and about 2/3 of the trajectories show the simultaneous breakage of the two C–N bonds.[10, 13]

Using femtosecond TOF mass spectrometry, the photodissociation dynamics of *trans*-azomethane in a molecular beam have been studied in this laboratory.[14] Real-time observation of the consecutive breakage of the two C–N bonds in azomethane has elucidated the nature of true concertedness on the femtosecond timescale—one must consider the characteristic time of nuclear motion in relation to the vibrational time ($\approx$ 30 fs) along the C–N bond-breaking reaction coordinate (RC); the rotational time of the entire molecule is much slower ($\approx$ a picosecond). In this full account of the early communication,[14] we provide details of experimental results with the pump – probe polarization at various configurations (parallel versus perpendicular) to examine the concept of concertedness and the dynamics further. High-level molecular orbital calculations were performed to characterize the PESs for the neutral and the cationic ground state using density functional theory (DFT), Gaussian-2 (G2),[24] and complete basis set (CBS)[25] approaches. The excited-state calculations were carried out using time-dependent (TD) DFT[26, 27] and CASSCF methods[28] with various basis functions.

2. Experimental and Theoretical Methods

The experimental setup for femtosecond pump and probe TOF mass spectrometry has been described in detail elsewhere.[29, 30] Briefly, the laser system consisted of a colliding-pulse mode-locked (CPM) laser pumped by an Ar^+ laser and then amplified by a four-stage, Nd:YAG-pumped amplifier operating at 20 Hz. The output of the femtosecond laser source had a pulse width of $\approx$ 80 fs with a pulse energy of $\approx$ 200 μJ at 615 nm. The pulse was split by a beam splitter to provide the pump and the probe beams. For the pump, the 615-nm output was frequency doubled. The probe beam was passed to a computer-controlled translation stage for the time delay. The polarization between the pump and the probe beams was varied by adjusting the orientation of a zero-order half-wave plate in the path of the

pump beam. The two beams were spatially combined and focused onto the supersonic molecular beam inside a vacuum chamber containing the TOF mass spectrometer. By gating the signal due to a particular ion and varying the delay time between the pump and the probe beam, the transient of each species was measured. *Trans*-azomethane was synthesized and purified according to a published procedure.[31] The molecular beam was formed by expanding gaseous *trans*-azomethane seeded in helium to give a total stagnation pressure of ≈20 psi.

The theoretical calculations for the ground-state PES were based on spin-unrestricted (U) DFT and CASSCF methods.[21a] Basically, the geometry of each species along the bond-breaking RC and the CNNC torsional coordinate was optimized using the UB3LYP hybrid functional[32, 33] with the 6-311G(d,p) basis set.[34] Since the S_0 azomethane is a closed-shell species, the spin-restricted (R) Kohn–Sham (KS) orbitals were implemented to describe the PES around the S_0 equilibrium region. As the C–N bond stretched, or the CNNC torsional angle rotated to an extent where the RKS and UKS descriptions started to differ, the UKS orbitals were used to better describe the bond dissociation process.[35] This spin-unrestricted DFT approach, though in principle suffers spin contamination from higher-multiplicity excited states, may well characterize the bond-dissociation as well as other isomerization PESs for azomethane and offer an economical alternative to other, more elaborate, multiconfiguration (MC) SCF and higher-order correlation methods.[35]

To describe the electronic structure for the open-shell species on the ground-state and the excited-state PESs of azomethane correctly, an MCSCF scheme was implemented using the CASSCF approach. The idea of CASSCF is to have a well-chosen active space and then perform full configuration interaction calculations inside the active space. Our strategy here was aimed at finding a proper active space that is capable of describing the C–N bond-dissociation and the *trans*-to-*cis* isomerization processes. Figure 1 shows the relevant molecular orbitals of azomethane for the *trans* (C_{2h}) and the *cis* (C_{2v}) isomers calculated at the B3LYP/6-311G(d,p) level of theory. The orbital correlation between both isomers along the CNNC torsional coordinate was made according to the textbook example of diimide.[36] Therefore, the active space should at least include six electrons distributed among four orbitals, abbreviated by CAS(6,4), to describe the PES along the rotational isomerization RC reasonably. We further demonstrate in Figure 2 the state-correlation diagram of the two isomers along the CNNC torsional coordinate calculated using the state-averaged (sa) CAS(6,7) method with the 6-311 + G(d,p) basis set; the extra Rydberg orbitals have been included in the active space. The geometries of the twisted configurations in different electronic states were optimized at the state-specific CAS(8,7)/cc-pVDZ level of theory, whereas the geometry of the S_0/S_1 CI was optimized at the state-averaged CAS(8,7)/cc-pVDZ level. To recover a significant dynamic correlation for each electronic state, the CASMP2 calculations were performed using the prior optimized CASSCF wavefunctions.[21c]

For all stationary points, vibrational frequencies were calculated at the same level of theory as the geometry optimization in order to determine the nature of the stationary points and to provide zero-point energy (ZPE) corrections for the PES. To confirm that the TS was the correct saddle point connecting two

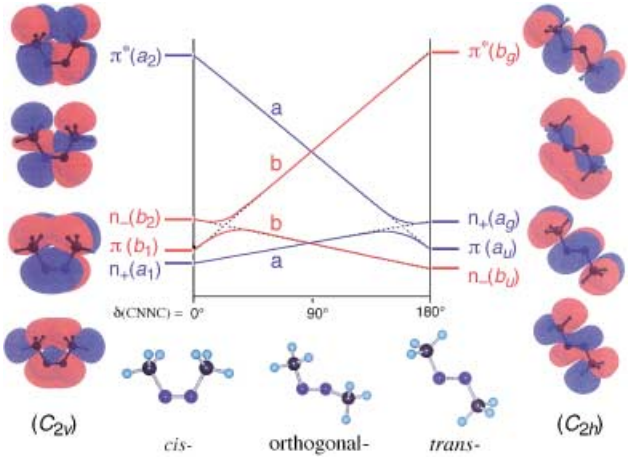

Figure 1. *Orbital-correlation diagram of* trans*-azomethane along the CNNC torsional reaction coordinate. Four relevant MOs of the* trans*- and* cis*- structures were calculated at the B3LYP/6-311G(d,p) level of theory.*

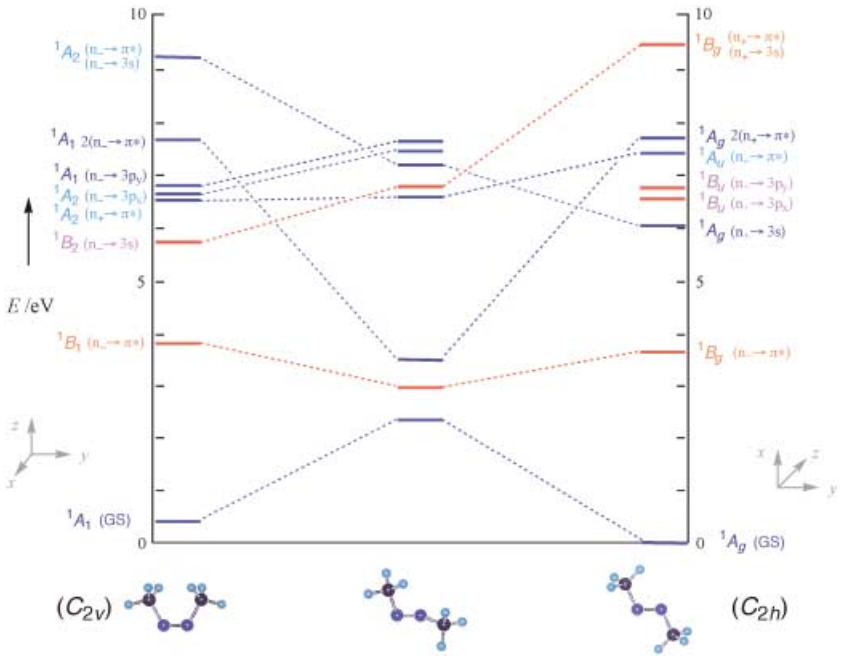

Figure 2. *State-correlation diagram of* trans*-azomethane along the CNNC torsional reaction coordinate. The excited states of the molecule in the* trans*-, the* cis*-, and the twisted configurations were calculated at the state-averaged CAS(6,7)/6-311 + G(d,p) level of theory and the relative energies are in electronvolts with respect to* trans*-azomethane.*

local minima, intrinsic reaction coordinate (IRC) calculations were performed. The absorption spectrum of AZM was constructed using the TDDFT approach with the vertical excitation energies and the oscillator strengths calculated at the TD-B3LYP/6-311++G(d,p), the TD-B3P86/6-311++G(d,p), and the TD-B3P86/6-311++G(3df,3pd) levels of theory.[26] All of the electronic structure calculations reported were performed using the Gaussian software package.[37]

3. Results and Data Analyses

Figure 3 shows the femtosecond-resolved mass spectrum of *trans*-azomethane, which is characterized by two major peaks at 58 amu and 43 amu corresponding to the parent ion ($CH_3N_2CH_3^+$) and the fragment ion ($CH_3N_2^+$), respectively; the

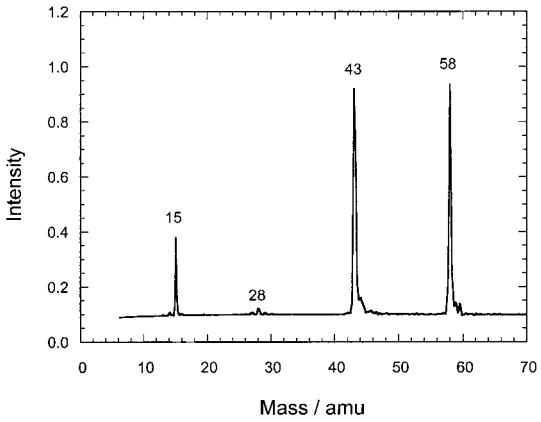

Figure 3. *Femtosecond mass spectrum of* trans*-azomethane. The spectrum was obtained at the perpendicular polarization with a delay time of ≈50 fs between the pump and the probe pulses.*

minor peaks at 28 amu and 15 amu are due to the ion fragments of N_2^+ and CH_3^+, respectively. Figure 4 displays the ion signals of the parent ion (58 amu) and the fragment ion (43 amu) as a

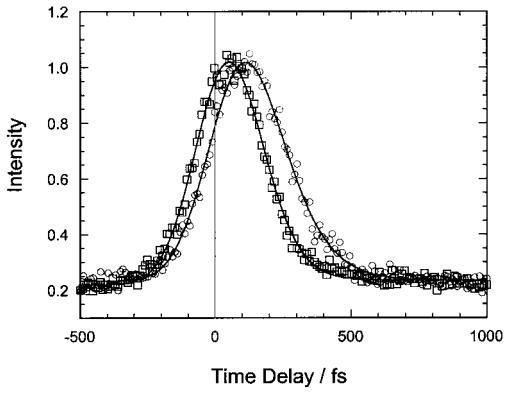

Figure 4. *Transients of* trans*-azomethane at 58 amu (□) and 43 amu (○) with the pump and the probe pulses at the perpendicular polarization. The solid curves are the fitted results with the convolution of the laser pulses.*

function of the delay time between the pump and the probe pulses, with the polarization of the femtosecond pulses in a perpendicular configuration. The parent transient (58 amu; shown as □) shows a very short-lived feature and it was fitted by a single exponential decay function with a time constant of 70 ± 10 fs; the convolution of the instrument response function (full width half maximum; FWHM = 180 fs) is included. The fragment transient (43 amu; shown as ○) shows apparently a different temporal feature in comparison with the parent signal, and it was fitted to a bi-exponential function with a rise time constant of 70 fs and a decay time constant of 100 ± 20 fs.

The parent signal (58 amu) at the maximum intensity (delay time ≈50 fs) is shown in Figure 5 as a function of the polarization angle between the pump and the probe pulses. The

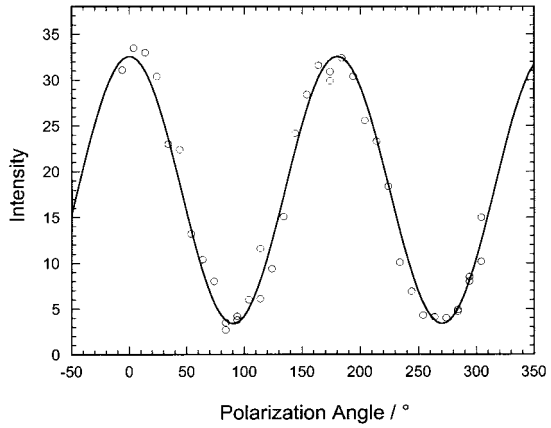

Figure 5. *Ion intensity of* trans*-azomethane at 58 amu as a function of the polarization angle between the pump and the probe pulses.*

intensity of the signal was found to vary drastically with the change in the polarization angles. In particular, the signal at the parallel polarization was enhanced by one order of magnitude in comparison with the signal at the perpendicular polarization. Moreover, the temporal behavior changed accordingly. The parent mass transient taken at the parallel polarization and the transient taken at the perpendicular polarization are shown in Figure 6. Note that the signal at the parallel polarization decayed with a longer time constant (100 fs) and in the opposite direction compared to the signal at the perpendicular polarization. It is concluded that the 307 nm and the 615 nm pulses must play different roles in the pump–probe experiments of different polarizations: The 307 nm pulse acts as a pump beam in the perpendicular polarization whereas the 615 nm pulse acts as a pump beam in the parallel polarization. It follows that one-photon pumping at 307 nm for the excitation of AZM to the $S_1(n,\pi^*)$ state, followed by ionization with at least three photons at 615 nm, is responsible for the transient signal observed for the perpendicular polarization. On the other hand, a two-photon absorption process at 615 nm, followed by two-photon ionization at 307 nm, results in the transient signal observed for the parallel polarization. Both excitation schemes are shown in Figure 7 together with the absorption spectra,[3, 18] the calculated

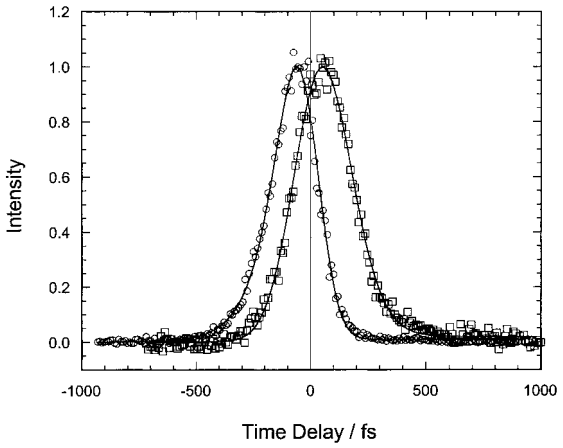

Figure 6. *Transients of* trans*-azomethane at 58 amu for the perpendicular (□) and the parallel (○) polarizations. The solid curves are the fitted results with the convolution of the laser pulses (see text).*

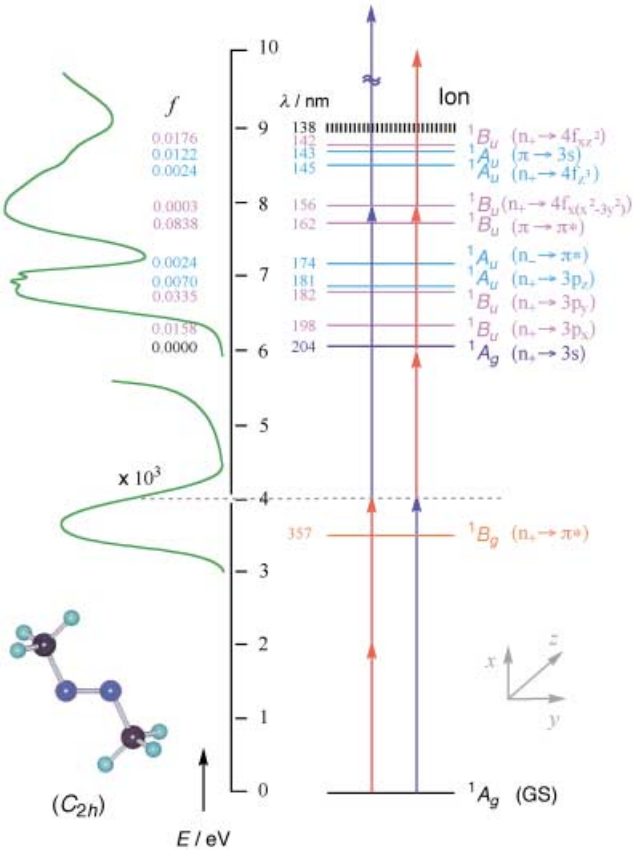

Figure 7. *The two pump – probe ionization schemes responsible for the observed transient signals of* trans*-azomethane at two different polarizations. The absorption spectra shown on the left side are the experimental results adopted from refs. [3, 18]. The vertical transitions and the corresponding oscillator strengths (f) were calculated using the TDDFT method at the B3P86/6-311++G(d,p) level of theory. The vertical excitation energies calculated at various levels of theory are summarized in Table 1.*

excited-state energies, and the corresponding oscillator strengths, which will be discussed in the following sections.

4. Theoretical Calculations

4.1. Vertical Excitation Energies

Table 1 lists the vertical excitation energies of AZM calculated at various levels of theory, and compares these with the results of Morokuma and co-workers[16] and the experimental electronic absorption spectrum.[3] The vertical excitation energy of the first excited state of AZM was calculated to be within the energy ranges of 3.47 – 3.49 eV and 3.72 – 3.74 eV using the TDDFT and the sa-CASSCF methods, respectively: Excellent agreement between the theoretical and experimental values was found. The values obtained at both the TD-B3LYP/6-311++G(d,p) and TD-B3P86/6-311++G(d,p) levels are only about 0.1 eV lower than the experimental value—the maximum intensity of the absorption spectrum of AZM due to the $S_0 \rightarrow S_1$ transition occurs at 340 nm (3.6 eV)[3]—whereas the values obtained from the high-level multiconfiguration methods are about 0.1 eV higher than the experimental value. We notice that the calculated S_1 vertical excitation energy at the sa-CAS(6,7) level is insensitive to the size of the basis functions from the cc-pVDZ to the 6-311+G(2df,p) basis sets (Table 1). Furthermore, the excellent agreement between the CASSCF results and the result obtained at the MRCISD(Q)/cc-pVTZ level (3.77 eV)[16] indicates that the additional dynamic electron correlation with numerous single and double excitations makes little or negligible improvement.

According to our theoretical calculations, the second excited state of AZM corresponds to a Rydberg state ($n_+ \rightarrow 3s$) with a symmetry-forbidden ($A_g \rightarrow A_g$) transition character. The vertical excitation energy of this 3s Rydberg state was determined to be 5.68 eV at the TD-B3LYP/6-311++G(d,p) level of theory, which is consistent with the experimental value (5.5 eV).[18] However, the energy values predicted at the TD-B3P86/6-311++G(d,p), the TD-B3P86/6-311++G(3df,3pd), the sa-CAS(6,7)/6-311+G(d,p), and the sa-CAS(6,7)/6-311+G(2df,p) levels are within the range of 6.01 – 6.09 eV and they overestimated the experimental value by $\approx$0.5 – 0.6 eV. The CASSCF calculations with different basis sets indicate that the diffuse functions on carbon and nitrogen atoms are essential in appropriately describing the excited states with Rydberg character, whereas the implementation of additional polarization functions on carbon and nitrogen atoms has very little effect on the prediction of the excited-state energies of AZM.

The vertical excitation energies of the other high-energy excited states of AZM have also been calculated using TDDFT (Table 1). For a general consideration of a highly symmetrical molecule with C_{2h} symmetry, the vertical excitations to the 3s and the 3d Rydberg states (belonging to either A_g or B_g symmetry) are strictly symmetry-forbidden, whereas the transitions to the 3p and 4f Rydberg states (A_u or B_u symmetry) are symmetry-allowed. Thus, only the 3p and some of the 4f Rydberg states below the ionization threshold ($\approx$9 eV) were considered to contribute to the high-energy electronic spectrum of AZM.[18] According to our TDDFT results calculated at both the TD-B3LYP and the TD-B3P86 levels, the three mysterious absorption bands of AZM in the excitation region of 6 – 9 eV, which were originally labeled as I, II, and III,[18] are now identified

Table 1. *Vertical excitation energies of* trans*-azomethane.*[a,b]

Electronic States	TD-B3LYP /++G(d,p)[e]	TD-B3P86 /++G(d,p)[e]	TD-B3P86 /++G(3df,3pd)[e]	sa-CAS(6,7) /cc-pVDZ	sa-CAS(6,7) /G(2df,p)[e]	sa-CAS(6,7) /+G(d,p)[e]	sa-CAS(6,7) /+G(2df,p)[e]	MRCI[c]/cc-pVTZ	Exp.[d]
$B_g(n_+ \rightarrow \pi^*)$	3.49	3.49	3.47	3.72	3.74	3.74	3.72	3.77	3.6
$A_g(n_+ \rightarrow 3s)$	5.68	6.08	6.09	8.77	8.16	6.04	6.01		5.5
$B_u(n_+ \rightarrow 3p_x)$	5.85	6.26	6.27			6.58	6.55		
$B_u(n_+ \rightarrow 3p_y)$	6.45	6.86	6.82			6.67	6.64		6.7
$A_u(n_+ \rightarrow 3p_z)$	6.46	6.91	6.87						
$A_g(n_+ \rightarrow 3d_{z^2})$	6.80	7.18	7.16						
$B_g(n_+ \rightarrow 3d_{yz})$	6.88	7.29	7.29						
$A_g(n_+ \rightarrow 3d_{xy})$	7.09	7.50	7.48						
$A_g(n_+ \rightarrow 3d_{x^2-y^2})$	7.76	8.18	8.09						
$B_g(n_+ \rightarrow 3d_{xz})$	8.11	8.48	8.41						
$B_u(n_+ \rightarrow 4f_{x(x^2-3y^2)})$	7.70	7.97	7.96						
$A_u(n_+ \rightarrow 4f_{z^3})$	8.22	8.61	8.57						
$B_u(n_+ \rightarrow 4f_{xz^2})$	8.48	8.84	8.75						8.6
$A_u(n_- \rightarrow \pi^*)$	7.13	7.16	7.13	7.45	7.42	7.47	7.46	7.31	
$B_u(\pi \rightarrow \pi^*)$	7.61	7.69	7.63	11.92	11.45			9.07	7.9
$B_g(\sigma \rightarrow \pi^*)$	8.15	8.16	8.12						
$A_u(\pi \rightarrow 3s)$	8.26	8.70	8.68	12.32	11.63				
$A_g(n_+,n_+ \rightarrow \pi^*,\pi^*)$				7.77	7.77	7.81	7.79		
$B_g(n_+,n_+ \rightarrow \pi^*,3s)$				12.30	11.63	9.51	9.48		

[a] All calculations are for the singlet states with the relative energies in electronvolts. [b] The molecular symmetry was restricted to C_{2h} with the *x*, *y*, and *z* coordinates as defined in Figure 7. [c] MRCISD(Q), reference wavefunction based on sa-CAS(6,4) calculations, adopted from [16]. [d] From refs. [3, 18]. [e] Pople-type triple-zeta basis function, that is, ++G(d,p) stands for the 6-311++G(d,p) basis set and so forth.

in Figure 7 as arising from the $n_+ \rightarrow 3p$, the $\pi \rightarrow \pi^*$, and the $n_+ \rightarrow 4f$ transitions, respectively. Note that these three absorption bands are mainly due to the excited states with B_u symmetry because the oscillator strengths of the B_u states were calculated to be substantially larger than those of the A_u states.

With the inclusion of the $3p_x(b_u)$ and $3p_y(b_u)$ orbitals in the active space, the excitation energies of the $B_u(n_+ \rightarrow 3p_x)$ and the $B_u(n_+ \rightarrow 3p_y)$ Rydberg states were also confirmed by the CASSCF calculations at the sa-CAS(6,7) level with the 6-311+G(d,p) and the 6-311+G(2df,p) basis sets (Table 1). The excitation energy of the second valence excited state, $A_u(n_- \rightarrow \pi^*)$, was calculated and consistent results between the TDDFT and the CASSCF/MRCI methods were obtained.[16] However, the $B_u(\pi \rightarrow \pi^*)$ valence excited state was predicted to lie above the ionization threshold at the MRCISD(Q)/cc-pVTZ level of theory.[16] Note that the dynamic electron correlation for the prediction of the excitation energy of the $B_u(\pi \rightarrow \pi^*)$ state was found to be substantially large (>2 eV) according to the results obtained from recent MRCI calculations,[16] suggesting that an even higher level of theory (maybe computationally very demanding) should be considered for the accurate characterization of this valence excited state. On the other hand, the good agreement between the TDDFT results (7.61 – 7.69 eV) and the experimental value (7.9 eV; band II)[18] is impressive, confirming the usefulness of this economical theoretical method (TDDFT) in predicting excitation energies for large molecules.

Although the current TDDFT results have successfully mapped out the electronic spectrum of AZM, excited states that involve more than one electronic excitation, such as the $A_g(n_+,n_+ \rightarrow \pi^*,\pi^*)$ and the $B_g(n_+,n_+ \rightarrow \pi^*,3s)$ states, cannot be calculated by the TDDFT method, due to the nature of the time-dependent linear response theory implemented by the method. These doubly excited states have to be computed using the CASSCF method. The predicted excitation energies of these doubly excited states and the other high-energy excited states are listed in Table 1.

4.2. Ground-State Potential Energy Surface

The ground-state PES of AZM has been well-characterized along both the isomerization and the dissociation pathways, and the corresponding reaction coordinate diagram is shown in Figure 8. Basically, the geometry of each ground-state species was fully optimized at the B3LYP/6-311G(d,p) level of theory and then single-point energy calculations were performed according to the additive schemes of the G2M(CC1)[24] and the CBS-RAD-(B3LYP,B3LYP)[25] methods. The results are summarized in Table 2. In general, both G2 and CBS calculations reproduced the experimental thermochemical values of AZM and thereby provided the energetics of AZM along the bond-breaking and isomerization coordinates of the ground-state PES. Although the results obtained from both methods have uncertainties of less than 0.8 kcal mol^{-1}, it is worth noting that the relatively cost-effective CBS-RAD method slightly outperformed the more costly G2M method.

Along the concerted bond-dissociation pathway of AZM, the synchronous bond-dissociation process involves an energy barrier of 51.9 kcal mol^{-1}, calculated at the CBS-RAD level. Along the stepwise bond-breaking pathway, the intermediate (CH_3N_2 radical) is formed, after the first C–N bond breakage, above the ground-state minimum by 51.9 kcal mol^{-1}. The CH_3N_2 radical should be short-lived once produced, because the energy barrier

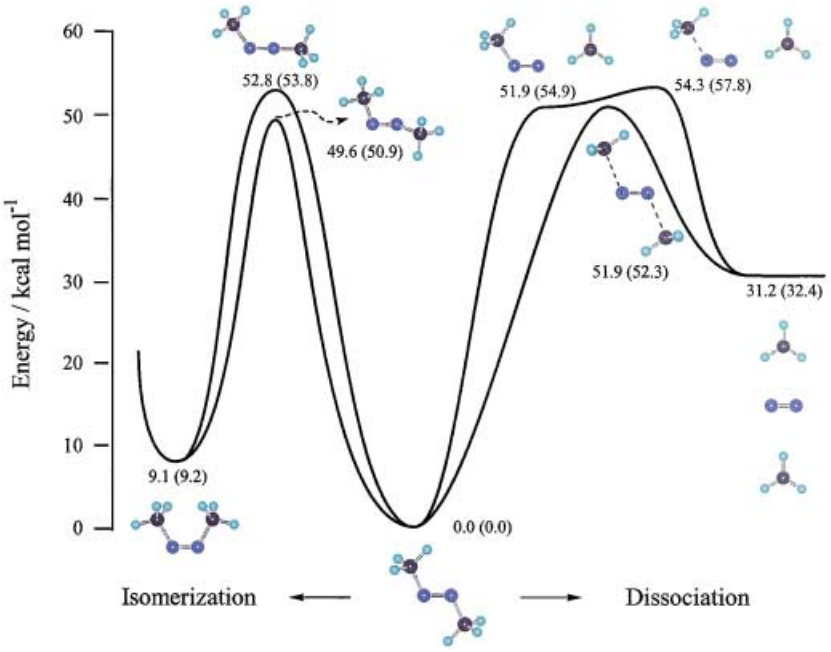

Figure 8. *Reaction coordinate diagram of* trans*-azomethane representing the global ground-state PES along different reaction channels. The stationary points shown in the diagram were characterized using the CBS-RAD(B3LYP,B3LYP)[25] method with the values shown in parentheses obtained from the G2M(CC1)[24] method. The corresponding structural parameters and the energetics are given in Table 2.*

of breaking the second C—N bond is only 2.4 kcal mol^{-1}. On the other hand, for the *trans*-to-*cis* isomerization reaction path, the energy barrier along the inversion (CNN bending) coordinate is 3.2 kcal mol^{-1} lower than the barrier along the rotation (CNNC torsional) coordinate, according to our CBS-RAD prediction.

Our high-level calculations indicate that both concerted and stepwise bond-breaking processes are competitive during the thermolysis of AZM on the ground-state PES. However, for the ultrafast photochemical processes we have to consider topological features of the excited-state surface that bring the excited state close to the ground state for an efficient electronic relaxation.

4.3. The S_0, S_1, T_1, and S_2 States at the Twisted Configurations

The orbital-correlation diagram of AZM along the CNNC torsional coordinate (Figure 1) shows a very strong HOMO – LUMO interaction at the geometry of the orthogonal configuration (δ(CNNC) $\approx 90^\circ$). The state-correlation diagram shown in Figure 2 further illustrates that three singlet states (labeled as S_0, S_1, and S_2) interact strongly in the twisted CNNC configuration. In the geometry near the orthogonal configuration, both the $S_0(^1A)$ and the $S_2(^1A)$ electronic states are strongly coupled with two paired electrons occupied in the nearly degenerate HOMO – LUMO (or n – π^*) pair. The $S_1(^1B)$ electronic state and its triplet counterpart, the $T_1(^3B)$ state are described by the electronic configuration with only one electron occupying each of the HOMO – LUMO pair. For appropriately describing these electronic states, we have employed the state-specific CASSCF approach with the additional multi-reference energy calculations using the CASMP2 method.[21]

The geometries of these four species (C_2 symmetry) were optimized at the CAS(8,7)/cc-pVDZ level of theory and the critical structural parameters are listed in Table 3. The values of the characteristic twisting parameter (the CNNC dihedral angle) were determined to be 92.8, 114.6, 100.0, and 96.2° for the $S_0(^1A)$, $S_1(^1B)$, $T_1(^3B)$, and $S_2(^1A)$ states, respectively. The frequency calculations at the same level have confirmed (as shown in Figure 2) that the $S_0(^1A)$ species is a transition state with only one imaginary frequency, whereas the $S_1(^1B)$, $T_1(^3B)$, and $S_2(^1A)$ species are local minima of the corresponding electronic states with all vibrational frequencies being positive (Table 4). Note that the $S_0(^1A)$ species represents the same rotamer as the TS 1 $\rightarrow$2 (^1A) species (Table 2) but the latter was characterized at the UB3LYP/6-311G(d,p) level of theory.

Table 2. *DFT-optimized structural parameters and high-correlated energies of relevant stationary points on the ground-state PES of azomethane.[a]*

	Distance [Å]		Angle [°]		Relative Energy[b] [kcal mol^{-1}]			
Species and Electronic States	*r*(NN)	*r*(CN)	θ(CNN)	δ(CNNC)	ΔE(DFT)[c]	ΔE(G2)[d]	ΔE(CBS)[e]	ΔE(exp)[f]
1, *trans*-AZM (^1A_g)	1.236	1.466	113.0	180.0	0.0[c]	0.0[d]	0.0[e]	0.0
2, *cis*-AZM ($^1A_1$)	1.237	1.483	120.2	0.0	10.1	9.2	9.1	9.1
3, CH_3N_2 ($^2A'$) + CH_3 ($^2A_2''$)	1.170	1.514	122.7		46.3	54.9	51.9	50.2 – 55.4
4, CH_3N_2 ($^2A''$) + CH_3 ($^2A_2''$)	1.178	1.404	180.0		71.1	81.4	78.2	
5, N_2 ($^1\Sigma_g^+$) + 2CH_3 ($^2A_2''$)	1.095				28.4	32.4	31.2	31.6
6, 2NCH_3 ($^3A''$)		1.414			102.0	116.0	114.0	
TS 1 $\rightarrow$**2** (^1A); rotamer	1.287	1.467	117.8	89.6	43.6	50.9	49.6	
TS 1 $\rightarrow$**2** ($^2A'$); invertomer	1.222	1.512	115.3		49.2	53.8	52.8	
		1.395	180.0					
TS 1 $\rightarrow$**5** (^1A_g)	1.133	2.126	112.3	180.0	50.0	52.3	51.9	
TS 3 $\rightarrow$**5** ($^2A'$) + CH_3 ($^2A_2''$)	1.135	1.820	119.6		47.9	57.8	54.3	

[a] Geometries and zero-point energies (ZPEs) were determined at the B3LYP/6-311G(d,p) level of theory. [b] Values are relative to the ground-state minimum (1) including the ZPE corrections. [c] B3LYP/6-311G(d,p); the reference total energy is -189.24401 hartree. [d] G2M(CC1); the reference total energy is -188.94196 hartree. [e] CBS-RAD(B3LYP,B3LYP); the reference total energy is -188.93439 hartree. [f] Ref.[4]

Table 3. *CASSCF-optimized structural parameters and CASMP2 energies for the S_0, S_1, T_1, and S_2 states of azomethane in twisted nuclear configurations.*[a]

Species and electronic configurations[b]	Distance [Å]		Angle [°]		Relative energy[c] [kcal mol^{-1}]			
	r(NN)	r(CN)	θ(CNN)	δ(CNNC)	ΔE(CASSCF)	ΔE(CASMP2)	ΔE(MRCI)[f]	$E_{00}+\Delta E$[g]
$S_0(^1A)$; $^1\lvert a^2\rvert-^1\lvert b^2\rvert$	1.371	1.461	111.4	92.8	−14.6	−17.5		51.5
$S_1(^1B)$; $^1\lvert ab\rvert$	1.278	1.447	123.0	114.6	0.0[d]	0.0[e]	0.0[f]	69.0
$T_1(^3B)$; $^3\lvert ab\rvert$	1.308	1.451	117.4	100.0	−24.4	−23.9	−24.0	45.1
$S_2(^1A)$; $^1\lvert a^2\rvert+^1\lvert b^2\rvert$	1.284	1.455	122.2	96.2	16.6	13.7		82.7

[a] Geometries (C_2 symmetry) and zero-point energies (ZPEs) were determined at the CAS(8,7)/cc-pVDZ level of theory; note $S_0(^1A)$ represents the same species as TS 1 → 2 (^1A); rotamer in Table 2. [b] The "a" and "b" represent the nearly degenerate HOMO – LUMO (or n – π*) pair with *A* and *B* symmetry, respectively; see Figure 1. [c] Values are relative to $S_1(^1B)$ including ZPE corrections scaled by 0.93.[41] [d] The reference total energy is −187.97066 hartree. [e] The reference total energy is −188.48324 hartree. [f] MRCISD(Q) with the CAS(6,4)/DZP reference wavefunction, adopted from ref. [16]; note that the reference total energy has been converted into −188.55151 hartree with the scaled ZPE correction according to the CAS(8,7)/cc-pVDZ calculation. [g] Energies relative to the S_0 minimum 1, *trans*-AZM (^1A_g); $\Delta E=\Delta E$(CASMP2) and $E_{00}=69.0$ kcal mol^{-1} (3.0 eV) according to the experimental result.[3]

Since the $S_1(^1B)$ species is a local minimum of the $S_1(n,\pi^*)$ state and its relative energy has been well determined from the 0 – 0 absorption band ($\lambda=415$ nm; 69 kcal mol^{-1} or ≈3 eV above the S_0 minimum),[3] we make a comparison for the relative energies of the other three species, with respect to the S_1 minimum, and the summary is in Table 3. The calculated relative energies of these species should be accurate for the following reasons. First, the uncertainty of the relative energy of the $T_1(^3B)$ species is only 0.1 kcal mol^{-1} at the CASMP2 level if it is compared with the MRCISD(Q) value. Second, if shifting the reference energy to the S_0 minimum (species 1 in Table 2), the relative energy of $S_0(^1A)$ was determined to be 51.5 kcal mol^{-1} at the CASMP2 level, which is in excellent agreement with the CBS-RAD value (51.9 kcal mol^{-1}) listed in Table 2. Thus, we expect the local minimum of the second excited singlet state, the $S_2(^1A)$ species, to be located above the ground-state minimum by 82.7 kcal mol^{-1} in the twisted nuclear configuration, according to our CASMP2 prediction.

Table 4. *Calculated vibrational frequencies of azomethane for the $S_0(^1A)$, $S_1(^1B)$, $T_1(^3B)$, and $S_2(^1A)$ species.*[a,b]

Mode	Description	$S_0(^1A)$	$S_1(^1B)$	$T_1(^3B)$	$S_2(^1A)$
ν_1(a)	CH stretch	3070	3066	3065	3070
ν_2(a)	CH stretch	3027	3008	3021	3003
ν_3(a)	CH stretch	2960	2944	2952	2936
ν_4(a)	CH_3 def.	1487	1508	1482	1733
ν_5(a)	CH_3 def.	1470	1470	1472	1488
ν_6(a)	CH_3 def.	1445	1464	1440	1461
ν_7(a)	CH_3 def.	1162	1436	1141	1447
ν_8(a)	CN symm. stretch	1045	880	1284	873
ν_9(a)	CH_3 def./NN stretch	823	1176	1104	1400
ν_{10}(a)	CH_3 def./NN stretch	773	1122	827	1136
ν_{11}(a)	CNN bend/CH_3 def.	309	445	314	653
ν_{12}(a)	CH_3 disrot. torsion	126	153	129	142
ν_{13}(a)	CNNC torsion	−1518[c]	123	174	264
ν_{14}(b)	CH stretch	3070	3066	3065	3070
ν_{15}(b)	CH stretch	3022	3008	3021	3002
ν_{16}(b)	CH stretch	2952	2940	2947	2930
ν_{17}(b)	CH_3 def.	1479	1478	1479	1471
ν_{18}(b)	CH_3 def.	1469	1466	1472	1466
ν_{19}(b)	CH_3 umbrella/CN stretch	1425	1432	1426	1421
ν_{20}(b)	CH_3 def.	1150	1150	1139	1137
ν_{21}(b)	CH_3 def.	1033	1104	1049	1100
ν_{22}(b)	CN asymm. stretch	865	1054	1062	1037
ν_{23}(b)	CNN bend/CH_3 def.	286	329	421	492
ν_{24}(b)	CH_3 conrot. torsion	111	149	158	148

[a] The values were obtained from state-specific CASSCF calculations at the CAS(8,7)/cc-pVDZ level. [b] All values are in cm^{-1} and are scaled by 0.93.[41] [c] The negative value corresponds to the imaginary frequency of the $S_0(^1A)$ species.

4.4. The Potential Energy Surfaces Along the Rotation Coordinate and the S_0/S_1 Conical Intersection

The relaxed surface-scan calculations on the S_1 PES were performed starting from the $S_1(^1B)$ structure with the geometry of each point on the surface optimized at the state-specific CAS(8,7)/cc-pVDZ level of theory, with a step-size of 5° along the CNNC torsional RC. The results are shown in Figure 9. Two topological features are shown for the S_1 PES along the torsional RC. First, there is no energy barrier involved, from the Franck – Condon region (torsional angle = 180°) down to the S_1 minimum area (torsional angle = 115°). Second, the S_0 surface goes up steeply along the torsional RC and reaches its maximum point at a torsional angle of ≈90° where the S_0 and the S_1 surfaces come close together. Since the S_1 minimum is located at a torsional angle of 115°, the crossing point between these two surfaces (S_0/S_1 CI) should be found at a torsional angle slightly above 90°. In fact, recent ab initio studies[16, 17e] have reported the optimized structure of the S_0/S_1 CI with a CNNC dihedral angle in the range of 92.8 – 93.8°. Using the sa-CASSCF method for the geometry optimized at the CAS(8,7)/cc-pVDZ level of theory, we have successfully located the S_0/S_1 CI at a torsional angle of δ(CNNC) = 93.1°.

The optimized structure and the two corresponding vectors, the gradient difference vector ($\mathbf{x_1}$), and the nonadiabatic coupling vector ($\mathbf{x_2}$) are shown in Figure 10. Two important points regarding the structure and the two vectors of the S_0/S_1 CI are the following: First, the structure of the S_0/S_1 CI is highly asymmetrical (C_1 symmetry) with the two C–N bond lengths equal to 1.439 and 1.528 Å, respectively. The two CNN bending angles are 127.5 and 112.2°, respectively. Second, the $\mathbf{x_1}$ and the $\mathbf{x_2}$ vectors indicate the possible reaction paths that can be followed on the S_0 PES after the molecule funnels through the CI. As shown in Figure 10, the nonadiabatic coupling vector $\mathbf{x_2}$ corresponds to a CNNC twisting motion that could lead to a

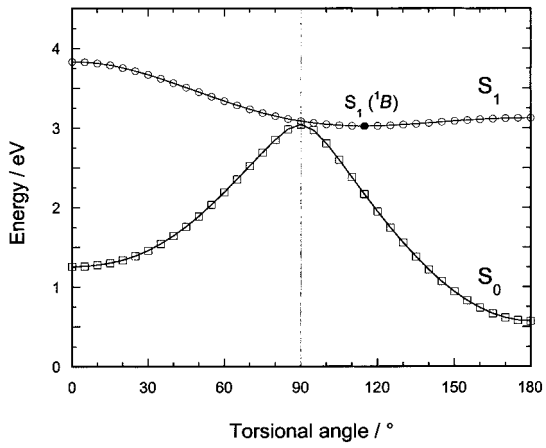

Figure 9. *Minimum energy pathway of azomethane optimized for the second root (the S_1 state) at the state-specific CAS(8,7)/cc-pVDZ level of theory along the CNNC torsional coordinate. The local minimum of the S_1 state is shown as $S_1(^1B)$ with the corresponding optimized parameters given in Table 3.*

trans-to-*cis* isomerization. On the other hand, the gradient difference vector $\mathbf{x}_1$ corresponds to an asymmetrical C—N bond stretching motion which results in the two C—N bonds breaking in an asynchronous manner. Such a structural and dynamical feature of the S_0/S_1 CI has a profound consequence in relation to the concept of concertedness, and this point will be discussed further in the Discussion Section.

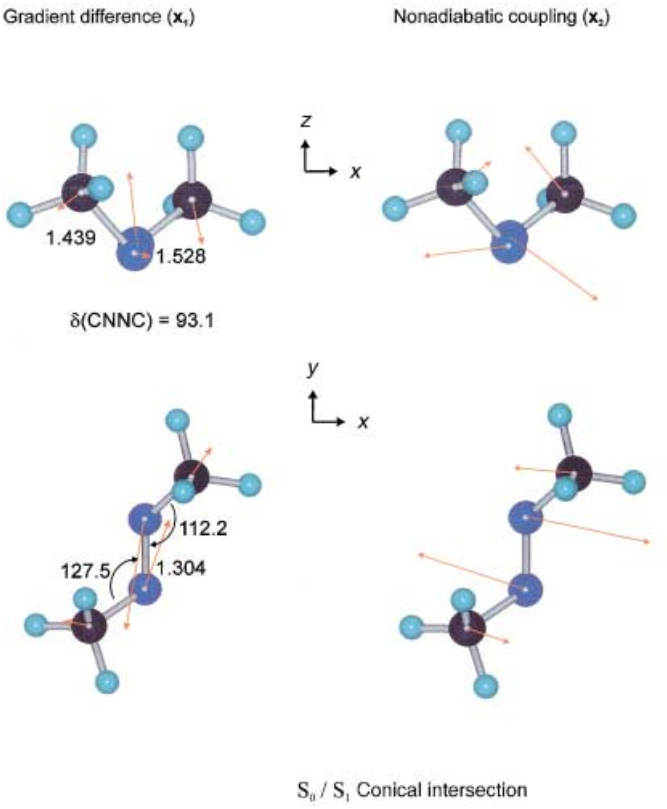

Figure 10. *The structure of the S_0/S_1 CI optimized at the state-averaged CAS(8,7)/cc-pVDZ level of theory with the corresponding bond lengths [Å] and bond angles [°] as indicated. The nonadiabatic coupling ($\mathbf{x}_2$) and the gradient difference ($\mathbf{x}_1$) vectors are shown.*

4.5. Ionization Potentials

The ground-state cationic potential surfaces of AZM along the bond-breaking and the torsional coordinates were characterized using the DFT approach at the spin-unrestricted B3LYP/6-311G(d,p) level of theory. Both the neutral and the ionic channels are shown in Figure 11 for comparison. For the ionic channel, the solid curve represents the relaxed (adiabatic) ionization potentials whereas the dashed curve represents the vertical ionization potentials with respect to the corresponding species in the neutral channel. The vertical ionization potential of AZM in the Franck – Condon structure was calculated to be 8.9 eV, which matches the result obtained from the MRCISD(Q) calculation[16] and is in good agreement with the experimental value (9.0 eV).[38] As for the adiabatic ionization potential, good agreement was also found between theory (8.2 eV) and experiment (8.3 eV).[38] The here reported ground-state cationic potential of AZM calculated at the B3LYP/6-311G(d,p) level should be accurate to within 0.1 eV.

One special character of the ionization potential (IP) curve of AZM is the large change of the potential energy along the CNN bending coordinate when breaking the first C—N bond. This change is because the $CH_3N_2^+$ species energetically prefers to have a linear CNN nuclear configuration. As a result, the

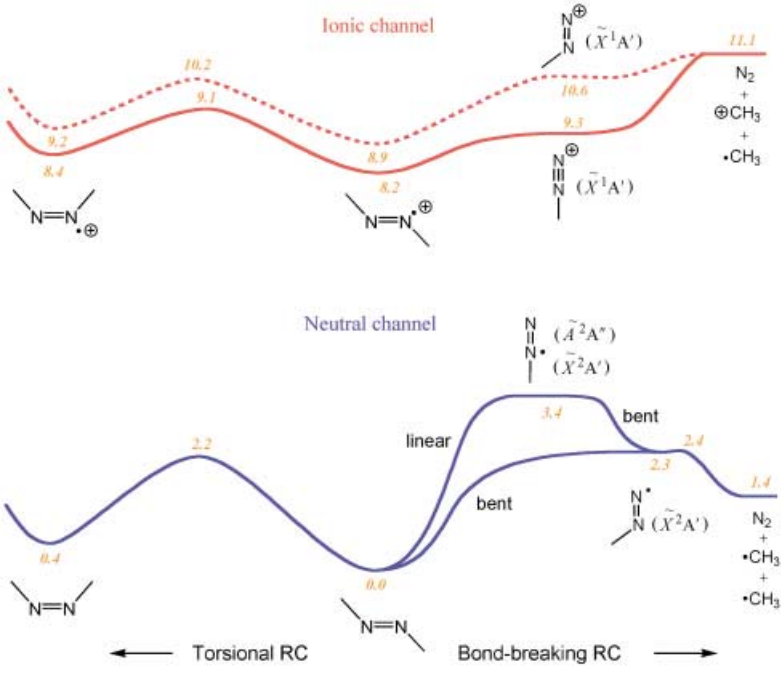

Figure 11. *Reaction coordinate diagrams of* trans*-azomethane representing the neutral and ionic channels along the bond-breaking (right side) and the torsional isomerization (left side) reaction path. The values shown in the diagram were characterized at the B3LYP/6-311G(d,p) level of theory.*

breaking of the first C–N bond from the AZM cation requires only 1.1 eV of internal energy in the parent cation, whereas further breaking of the second C–N bond needs an extra 1.8 eV of internal energy in the $CH_3N_2^+$ species (Figure 11). This linear structural feature of $CH_3N_2^+$ is very similar to that of the isoelectronic cation (CH_3CO^+) produced from the acetone parent cation.[21c] In fact, not only the ionic state but also the other low-lying electronic excited states of the CH_3N_2 species have a linear CNN geometry and their potential curves along the CNN bending RC predicted at the TD-B3P86/6-311++G(d,p) level are shown in Figure 12.

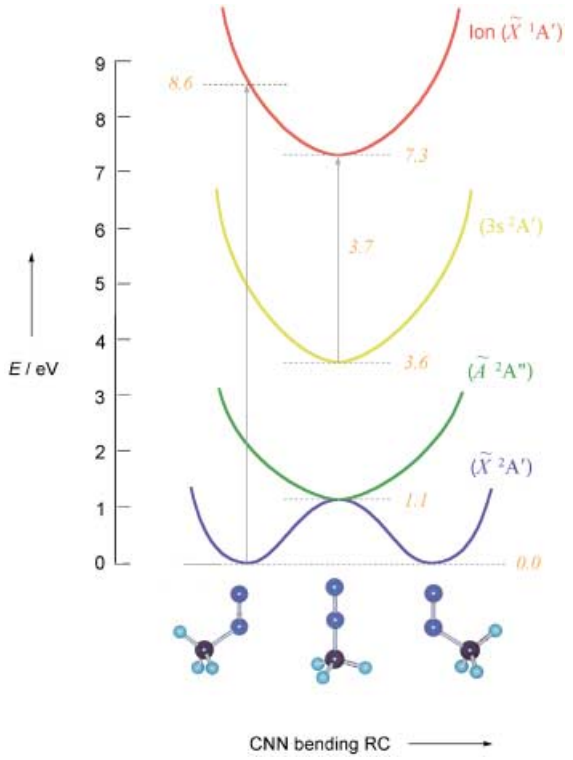

Figure 12. *The potential energy curves of the CH_3N_2 radical along the CNN bending coordinate. The curves were constructed from the vertical excitation energies calculated at the TD-B3P86/6-311++G(d,p) level of theory and are based on the bent ($\tilde{X}^2A'$) and the linear ($\tilde{A}^2A''$) geometries optimized at the B3LYP/6-311G(d,p) level of theory.*

5. Discussion

Because the transient signal shows an opposite decay feature for the UV (307 nm) and the visible (615 nm) pulses at the parallel and the perpendicular polarizations, and the amplitude changes with the polarization angle (Figure 5), we were able to time-order the pump and probe pulses. As indicated in Figure 7, the ion signal observed for the perpendicular polarization is due to a one-photon pumping process at 307 nm followed by ionization with at least three photons at 615 nm; the signal observed for the parallel polarization is due to a two-photon absorption at 615 nm followed by two-photon ionization at 307 nm. The theoretical foundation for the assignment of these excitation/ionization schemes is consistent with the experimental observations.

Since ground-state AZM belongs to the C_{2h} point group, the $^1A_g(GS) \rightarrow {}^1B_g(n_+ \rightarrow \pi^*)$ transition is strictly symmetry-forbidden. In order for the forbidden n – π* transition to occur, an "intensity-borrowing" mechanism must be invoked through an appropriate vibronic coupling process.[21a] If the intensity is borrowed from an upper A_u state, the transition dipole moment of the pump pulse ($\hat{\mu}_{pu}$) will be along the *z* axis, perpendicular to the molecular plane. On the other hand, if a B_u state is involved, the $\hat{\mu}_{pu}$ will be in the *xy* molecular plane. To a first-order approximation, the intensity borrowed from the allowed state of A_u or B_u symmetry would require vibrational motion (Q) dictated by the matrix element $\langle B_g | Q | A_u \rangle$ or $\langle B_g | Q | B_u \rangle$, respectively; the total product must be totally symmetric. Therefore, Q should correspond to a vibrational motion with B_u or A_u symmetry.

According to our TDDFT calculation (Figure 7), a 3p Rydberg state with B_u symmetry should be responsible for the intensity-borrowing mechanism of the forbidden $^1A_g \rightarrow {}^1B_g$ transition initiated by the 307 nm pump pulse ($\hat{\mu}_{pu}$ in the *xy* molecular plane). The $^1B_g \rightarrow {}^1B_u$ transition by the probe pulse of 615 nm is symmetry-allowed, and this has a transition dipole of A_u symmetry [$\hat{\mu}_{pr}(z)$]. Accordingly, this (1 + 3) REMPI scheme (one-photon excitation with *xy* plane polarization plus three-photon ionization with *z*-axis polarization) is consistent with our observation at the perpendicular polarization condition. On the other hand, the $^1A_g \rightarrow {}^1B_g$ transition is symmetry-allowed for a two-photon excitation induced by the pump pulse at 615 nm [$\hat{\mu}_{pu}(z)$]. The $^1B_g \rightarrow {}^1B_u$ transition induced by the probe pulse of 307 nm will lead to $\hat{\mu}_{pr}$ that is parallel to the *z* axis. This (2 + 2) process (two-photon excitation with *z* axis polarization plus two-photon ionization also with *z* axis polarization) is again consistent with the experimental observations for the parallel polarization conditions. These two different excitation/ionization schemes also explain the fact that the intensity observed for parallel polarization was one order of magnitude stronger than the intensity observed for perpendicular polarization (Figure 5). For the experiments carried out in the perpendicular polarization geometry, the above excitation/ionization scheme was also confirmed by the study of the power-dependence at $\lambda_{pu} =$ 307 nm, a one-photon process.[14]

From these studies, we conclude that the observed transient behavior for the parent mass (58 amu) and the fragment mass (43 amu) reflects the femtosecond dissociation dynamics of AZM on the S_1 PES. Because the parent signal decays in 70 fs, the electronic relaxation of the excited AZM from the S_1 PES must occur during this time scale. The intensity-borrowing involves a vibrational motion with A_u symmetry, and our theoretical calculations indicate that this A_u vibration corresponds to a torsional motion; the minimum of the $S_1(n,\pi^*)$ state has a structure with a CNNC dihedral angle of $\approx 115^\circ$ (Table 3), and there is no energy barrier along the CNNC torsional RC toward the minimum region on the S_1 PES (Figure 9). This is consistent with ultrafast $S_1 \rightarrow S_0$ IC process on the femtosecond time scale. For the parallel polarization, the observed decay time constant of the parent signal is longer than that for the perpendicular geometry (100 fs versus 70 fs), which is not surprising because

the former involves a two-photon symmetry-allowed transition and the driving force towards the S_1 minimum region along the torsional RC is not as strongly biased as that through the vibration involved in the vibronic coupling.

A recent experimental study using the PTS technique has reported an isotropic angular distribution ($\beta \approx 0$) of the CH_3 and the N_2 fragments, and has suggested that the lifetime of excited AZM may be longer than its rotational period (≈a picosecond).[10] However, the PTS study at 193 nm by Huber and coworkers[11] pointed out that the lack of anisotropy may be due to a geometric effect caused by a particular orientation of the electronic transition moment $\hat{\mu}_{pu}$; the anisotropy parameter vanishes if the angle between $\hat{\mu}_{pu}$ and the direction of the fragment recoil velocity is close to the magic angle (54.7°). This condition is easily met if $\hat{\mu}_{pu}$ is oriented parallel or near parallel to the N=N bond (the *y* axis) of the parent molecule, so that the ejection of the first CH_3 fragment would occur at an orientation close to the magic angle; this "magic-angle condition" would persist even when the excited molecule twisted along the CNNC torsional RC prior to the first C–N bond dissociation. The geometric picture is consistent with the results obtained from both the time-resolved study[14] and the energy-resolved experiments,[10, 11, 13] and supports our conclusion regarding the time scale for the nuclear motion.

The observed rise (70 fs) and decay (100 fs) dynamical feature for the fragment mass (43 amu) at the perpendicular polarization is in accord with the formation of a short-lived CH_3N_2 intermediate. The mechanism of the ultrafast C–N bond-dissociation process is explained as follows: The forbidden n – π* transition borrows intensity from the upper B_u state and utilizes the ultrafast A_u torsional motion which also takes the molecule toward the S_1 minimum region. As shown in Figure 9, the S_1 and S_0 potential curves approach each other along the CNNC torsional RC and the two surfaces are closest at a torsional angle close to 90°. The S_1 molecule must efficiently find the S_0/S_1 CI guided by the torsional driving force. Funneling through the CI is a very efficient process[39, 40] and therefore it leads to the breakage of the first C–N bond in less than a C–N stretching vibrational period (Table 4; $\nu_{22} = 1054\ cm^{-1}$ corresponds to a period of ≈30 fs) for the motion driven by the force following the gradient difference vector ($\mathbf{x}_1$) direction (Figure 10). Note that the $\mathbf{x}_1$ vector of the S_0/S_1 CI shown in Figure 10 corresponds to an asymmetric vibration with a combined C–N stretching and the CCN bending motion, which results in the consecutive bond breakage in a very short time and on the ground-state surface. This dynamic picture is consistent with our real-time observations of the parent and intermediate.

The involvement of the CNN bending motion during the first C–N bond cleavage has a significant effect on lowering the ionization potential for the observation of the short-lived CH_3N_2 species. Our DFT calculations at the B3LYP/6-311G(d,p) level (Figure 11) give the IP of the bent CH_3N_2 radical to be 8.3 eV, whereas the IP of the linear CH_3N_2 species is only 5.9 eV, which is less than the energy of three photons at $\lambda_{pr} = 615$ nm for the ionization. The bending CNN motion is also important for the second bond breakage. The observed 100 fs lifetime of the CH_3N_2 intermediate is not only consistent with the low energy barrier (≈0.1 eV; Figure 8) involved along the second C–N bond-breaking RC but also reflects the "memory" of the asymmetric C–N stretching motion after going through the S_0/S_1 CI in the first C–N bond breakage. Finally, we note that at the parallel polarization geometry, the excess energy in the parent cation is expected to be much above the fragmentation threshold (Figure 11) for two probe photons at 307 nm (Figure 7). The transient signal shown for the fragment mass (43 amu) at this parallel polarization comes mainly from the energetic parent ion species and the corresponding dynamics of the CH_3N_2 intermediate become more difficult to resolve.

6. Conclusion

Although the thermal decomposition of azomethane may produce methyl radicals by concerted (or asynchronous) and consecutive reaction pathways, the photochemistry is very different in its elementary steps. The combination of the real-time observations and theoretical calculations described above elucidates the mechanism for the ultrafast dinitrogen extrusion and the overall picture is summarized in Scheme 2. Upon excitation to the $S_1(n,\pi^*)$ state with one photon at 307 nm, the initial driving force on the S_1 PES is the CNNC torsional motion involved in the vibronic coupling of the state and is facilitated by the n – π* electronic excitation. The symmetry of the excited molecule must change from the C_{2h} symmetry of the Franck–Condon geometry to the C_2 symmetry along the torsional RC. This way the S_0/S_1 CI near the S_1 minimum region can be reached with further reduction of the molecular symmetry from C_2 to C_1. After funneling through the S_0/S_1 CI, the motion becomes significant in the asymmetric C–N stretch via the direction of the

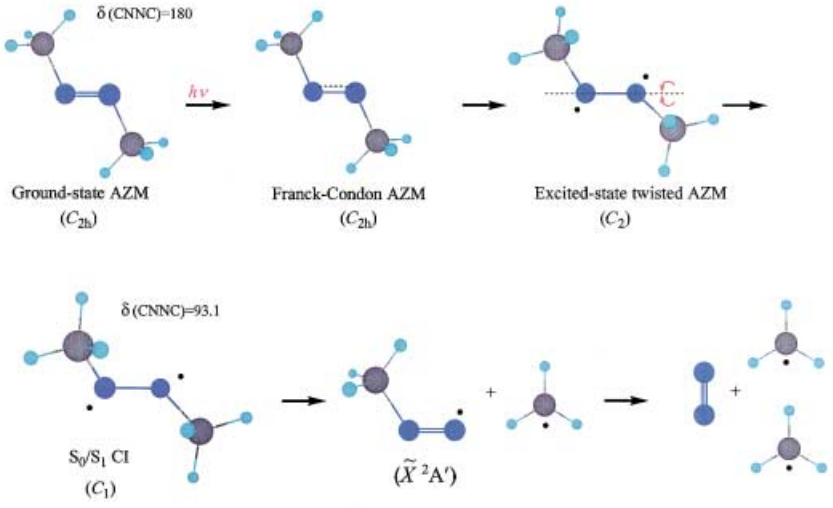

Scheme 2. *Dinitrogen extrusion mechanism of azomethane.*

gradient difference vector of the CI on the S_0 PES. Hence, the cleavage of the first C–N bond on the femtosecond time scale. The second C–N bond cleavage occurs consecutively (with a small barrier) in the observed 100 fs. This picture is consistent with the polarization anisotropy, power dependencies, and theoretical calculations of the ground, excited, and ion potential energy surfaces. The concept of concertedness can only be established if the time scale of bond breakage is compared with the vibrational dynamics, otherwise the operational definition may be challenged due to slow rotational clocking and/or accidental geometry relationship between the transition moment and the direction of recoil. As a final note, any collision present in gas cell experiments may lead to erroneous results because of the involvement of dissociation and isomerization pathways on the global energy surface.

This work was supported by the Office of Naval Research and the US Air Force Office of Scientific Research. We thank Dr. O. K. Abou-Zied and Prof. A. A. Scala for their contributions in the initial phase of the work. E.W.D. thanks Prof. Ching-Han Hu for many helpful discussions and the National Science Council of the Republic of China for the support through NSC 91-2113-M-009-008.

[1] C. V. Cannon, O. K. Rice, *J. Am. Chem. Soc.* **1941**, *63*, 2900 – 2905.
[2] M. H. Jones, E. W. R. Steacie, *J. Chem. Phys.* **1953**, *21*, 1018 – 1025.
[3] S. S. Collier, D. H. Slater, J. G. Carvert, *Photochem. Photobiol.* **1968**, *7*, 737 – 753.
[4] P. S. Engel, *Chem. Rev.* **1980**, *80*, 99 – 150, and references therein.
[5] J. E. Baggott, M. Brouard, M. A. Coles, A. Davis, P. D. Lightfoot, M. T. Macpherson, M. J. Milling, *J. Phys. Chem.* **1987**, *21*, 317 – 322.
[6] P. Chuang, Y. L. Chan, C. H. Chuang, S.-H. Chien, T. J. Chuang, *App. Surf. Sci.* **2001**, *169*, 153 – 159.
[7] K. N. Houk, Y. Li, J. D. Evanseck, *Angew. Chem.* **1992**, *104*, 711 – 737; *Angew. Chem. Int. Ed. Engl.* **1992**, *31*, 682 – 708.
[8] J. A. Berson, *Science* **1994**, *266*, 1338 – 1339.
[9] a) K. A. Burton, R. B. Weisman, *J. Am. Chem. Soc.* **1990**, *112*, 1804 – 1807; b) B. K. Andrews, K. A. Burton, R. B. Weisman, *J. Chem. Phys.* **1992**, *96*, 1111 – 1120.
[10] S. W. North, C. A. Longfellow, Y. T. Lee, *J. Chem. Phys.* **1993**, *99*, 4423 – 4429.
[11] T. Gejo, P. Felder, J. R. Huber, *Chem. Phys.* **1995**, *195*, 423 – 433.
[12] D. H. Fairbrother, K. A. Dickens, P. C. Stair, E. Weitz, *Chem. Phys. Lett.* **1995**, *246*, 513 – 520.
[13] A. S. Bracker, S. W. North, A. G. Suits, Y. T. Lee, *J. Chem. Phys.* **1998**, *109*, 7238 – 7245.
[14] E. W.-G. Diau, O. K. Abou-Zied, A. A. Scala, A. H. Zewail, *J. Am. Chem. Soc.* **1998**, *120*, 3245 – 3246.
[15] C.-H. Hu, H. F. Schaefer, III, *J. Phys. Chem.* **1995**, *99*, 7507 – 7513.
[16] R. Liu, Q. Cui, K. M. Dunn, K. Morokuma, *J. Chem. Phys.* **1996**, *105*, 2333 – 2345.
[17] a) P. Cattaneo, M. Persico, *Chem. Phys.* **1997**, *214*, 49 – 60; b) P. Cattaneo, M. Persico, *Chem. Phys. Lett.* **1998**, *289*, 160 – 166; c) P. Cattaneo, M. Persico, A. Tani, *Chem. Phys.* **1999**, *246*, 315 – 322; d) P. Cattaneo, G. Granucci, M. Persico, *J. Phys. Chem. A* **1999**, *103*, 3364 – 3371; e) P. Cattaneo, M. Persico, *Theor. Chem. Acc.* **2000**, *103*, 390 – 398; f) P. Cattaneo, M. Persico, *J. Am. Chem. Soc.* **2001**, *123*, 7638 – 7645.
[18] M. B. Robin, R. R. Hart, N. A. Kuebler, *J. Am. Chem. Soc.* **1967**, *89*, 1564 – 1572.
[19] R. N. Camp, I. R. Epstein, C. Steel, *J. Am. Chem. Soc.* **1977**, *99*, 2453 – 2459.
[20] H. Rau, *Angew. Chem.* **1973**, *85*, 248 – 258; *Angew. Chem. Int. Ed. Engl.* **1973**, *12*, 224 – 235.
[21] See, for example,a) E. W.-G. Diau, C. Kotting, A. H. Zewail, *ChemPhysChem* **2001**, *2*, 273 – 293; b) E. W.-G. Diau, C. Kötting, A. H. Zewail, *ChemPhysChem* **2001**, *2*, 294 – 309; c) E. W.-G. Diau, C. Kötting, T. I. Sølling, A. H. Zewail, *ChemPhysChem* **2002**, *3*, 57 – 78; d) T. I. Sølling, E. W.-G. Diau, C. Kötting, S. De Feyter, A. H. Zewail, *ChemPhysChem* **2002**, *3*, 79 – 97, and references therein.
[22] C. E. M. Strauss, P. L. Houston, *J. Phys. Chem.* **1990**, *94*, 8751 – 8762.
[23] S. W. North, D. A. Blank, J. D. Gezelter, C. A. Longfellow, Y. T. Lee, *J. Chem. Phys.* **1995**, *102*, 4447 – 4460.
[24] A. M. Mebel, K. Morokuma, M. C. Lin, *J. Chem. Phys.* **1995**, *103*, 7414 – 7421.
[25] P. M. Mayer, C. J. Parkinson, D. M. Smith, L. Radom, *J. Chem. Phys.* **1998**, *108*, 604 – 615.
[26] K. B. Wiberg, R. E. Stratmann, M. J. Frisch, *Chem. Phys. Lett.* **1998**, *297*, 60 – 64.
[27] D. J. Tozer, N. C. Handy, *Phys. Chem. Chem. Phys.* **2000**, *2*, 2117 – 2121.
[28] M. Merchan, B. O. Roos, R. McDiardmid, X. Xing, *J. Chem. Phys.* **1996**, *104*, 1791 – 1804.
[29] A. H. Zewail, *Femtochemistry: Ultrafast Dynamics of the Chemical Bond, Vol.I and II*, World Scientific, Singapore, **1994**, and references therein.
[30] E. W.-G. Diau, S. De Feyter, A. H. Zewail, *J. Chem. Phys.* **1999**, *110*, 9785 – 9788.
[31] P. S. Engel, R. A. Melaugh, M. Mansson, J. W. Timberlake, A. W. Garner, F. D. Rossini, *J. Chem. Thermodynamics* **1976**, *8*, 607 – 621.
[32] A. D. Becke, *J. Chem. Phys.* **1993**, *98*, 5648 – 5652.
[33] C. Lee, W. Yang, R. G. Parr, *Phys. Rev. B* **1988**, *37*, 785 – 789.
[34] W. J. Hehre, L. Radom, P. v. R. Schleyer, J. A. Pople, *Ab Initio Molecular Orbital Theory*, Wiley, New York, **1986**.
[35] F. Jensen, *Introduction to Computational Quantum Chemistry*, John Wiley & Sons, New York, **1998**.
[36] M.Klessinger, J. Michl, *Excited States and Photochemistry of Organic Molecules*, VCH, New York, **1995**, p. 376.
[37] Gaussian 98 (Revision A.7), M. J. Frisch, G. W. Trucks, H. B. Schlegel, G. E. Scuseria, M. A. Robb, J. R. Cheeseman, V. G. Zakrzewski, J. A. Montgomery, R. E. Stratmann, J. C. Burant, S. Dapprich, J. M. Millam, A. D. Daniels, K. N. Kudin, M. C. Strain, O. Farkas, J. Tomasi, V. Barone, M. Cossi, R. Cammi, B. Mennucci, C. Pomelli, C. Adamo, S. Clifford, J. Ochterski, G. A. Petersson, P. Y. Ayala, Q. Cui, K. Morokuma, D. K. Malick, A. D. Rabuck, K. Raghavachari, J. B. Foresman, J. Cioslowski, J. V. Ortiz, B. B. Stefanov, G. Liu, A. Liashenko, P. Piskorz, I. Komaromi, R. Gomperts, R. L. Martin, D. J. Fox, T. Keith, M. A. Al-Laham, C. Y. Peng, A. Nanayakkara, C. Gonzalez, M. Challacombe, P. M. W. Gill, B. G. Johnson, W. Chen, M. W. Wong, J. L. Andres, M. Head-Gordon, E. S. Replogle, J. A. Pople, Gaussian, Inc., Pittsburgh, PA, **1998**.
[38] D. C. Frost, S. T. Lee, C. A. McDowell, N. P. C. Westwood, *J. Chem. Phys.* **1976**, *64*, 4719 – 4729.
[39] W. Domcke, G. Stock, *Adv. Chem. Phys.* **1997**, *100*, 1 – 169.
[40] F. Bernardi, M. Olivucci, M. A. Robb, *Chem. Soc. Rev.* **1996**, *25*, 321 – 328, and references therein.
[41] D. W. Liao, A. M. Mebel, M. Hayashi, Y. J. Shiu, Y. T. Chen, S. H. Lin, *J. Chem. Phys.* **1999**, *111*, 205 – 215.

Received: November 11, 2002 [F 579]

